

Simulations for single-dish intensity mapping experiments

M.-A. Bigot-Sazy,^{1*} C. Dickinson,^{1†} R.A. Battye,¹ I.W.A. Browne,¹
Y.-Z. Ma,¹ B. Maffei,¹ F. Noviello,¹ M. Remazeilles,¹ P.N. Wilkinson¹

¹Jodrell Bank Centre for Astrophysics, Alan Turing Building, School of Physics & Astronomy, The University of Manchester, Oxford Road, Manchester M13 9PL, UK

20 December 2021

ABSTRACT

HI intensity mapping is an emerging tool to probe dark energy. Observations of the redshifted HI signal will be contaminated by instrumental noise, atmospheric and Galactic foregrounds. The latter is expected to be four orders of magnitude brighter than the HI emission we wish to detect. We present a simulation of single-dish observations including an instrumental noise model with $1/f$ and white noise, and sky emission with a diffuse Galactic foreground and HI emission. We consider two foreground cleaning methods: spectral parametric fitting and principal component analysis. For a smooth frequency spectrum of the foreground and instrumental effects, we find that the parametric fitting method provides residuals that are still contaminated by foreground and $1/f$ noise, but the principal component analysis can remove this contamination down to the thermal noise level. This method is robust for a range of different models of foreground and noise, and so constitutes a promising way to recover the HI signal from the data. However, it induces a leakage of the cosmological signal into the subtracted foreground of around 5%. The efficiency of the component separation methods depends heavily on the smoothness of the frequency spectrum of the foreground and the $1/f$ noise. We find that as, long as the spectral variations over the band are slow compared to the channel width, the foreground cleaning method still works.

Key words: diffuse radiation – large-scale structure of Universe – cosmology: observations – methods: statistical – radio continuum: general, galaxies – radio lines: galaxies, ISM

1 INTRODUCTION

One of the main challenges of modern cosmology is to explain the late-time acceleration of the expansion of the Universe. There are several independent methods to probe dark energy: Baryonic Acoustic Oscillations (BAOs), weak and strong gravitational lensing, cluster counts and supernovae. However, BAO measurements appear to be the most powerful cosmological tool at low redshift because they are limited by statistical rather than systematics errors. Using the BAOs as a standard ruler measures the expansion of the Universe as a function of redshift, and so constrains the properties of dark energy (e.g. Weinberg et al. 2013).

A complementary method to the usual large optical surveys of galaxies to study BAOs is HI intensity mapping (Battye, Davies & Weller 2004; Peterson, Bandura & Pen 2006; Chang et al. 2008; Loeb & Wyithe 2008; Peterson et al. 2009). This method aims to give a tomographic distribution of the neutral HI emission present in the recent Universe over large angular scales. Simulations indicate that the HI intensity mapping technique will give very precise

constraints on cosmological parameters, and in particular, on the dark energy equation of state at low redshift (Chang et al. 2008), and at high redshift (McQuinn et al. 2006; Bowman, Morales & Hewitt 2007; Mao et al. 2008). This sensitivity comes from the large volume of the survey.

Some HI experiments are currently underway such as BAO-radio¹, BINGO², CHIME³, FAST⁴, TIANLAI⁵. Using intensity mapping, the Green Bank Telescope (GBT)⁶ has provided the first detection of the HI signal at $z \sim 0.8$ cross-correlated with the WiggleZ Dark Energy Survey (Masui et al. 2013). This detection shows the HI intensity mapping as a promising tool and gives a lower limit on the fluctuations power of the HI signal. The first phase of the SKA instrument will be built in the next decade and it will offer a broad range of frequencies and a large survey area. Thus, this

* E-mail: marie-anne.bigot-sazy@manchester.ac.uk

† E-mail: clive.dickinson@manchester.ac.uk

¹ <http://arxiv.org/pdf/1209.3266v1.pdf>

² <http://www.jb.man.ac.uk/research/BINGO/>

³ <http://chime.phas.ubc.ca/>

⁴ <http://fast.bao.ac.cn/en/>

⁵ <http://tianlai.bao.ac.cn/>

⁶ <https://science.nrao.edu/facilities/gbt/>

instrument has great potential to deliver maps of the HI intensity (Bull et al. 2015).

To convert the promise into reality radio observations will have to deal with different contaminants, which can dominate the signal of interest in the data, such as astrophysical foregrounds, radio frequency interference (RFI) and instrumental noise. Another important contaminant is time variable noise introduced during propagation of the signal through the atmosphere, which gives an additional contribution to the $1/f$ noise of the instrument. The amplitude of the atmospheric effects depends on the observing frequency, on the elevation of the instrument above sea level and on the instantaneous weather conditions.

The most important challenge for any intensity mapping experiment is the control of foreground emissions. Thus, the data analysis must include a robust foreground subtraction algorithm. At ~ 1 GHz, the most relevant foregrounds are a combination of Galactic emission, mostly synchrotron, and that from the background of extragalactic point sources. See, for example, the discussion in Battye et al. (2013). These emissions are at least four orders of magnitude larger ($T_b \sim 1000$ mK) than the HI signal fluctuations ($\delta T_b \sim 1$ mK). In order to subtract the foreground, the high spectral resolution offered by any HI experiment allows us to exploit the frequency information. In particular the spectra of the foregrounds are expected to be smooth and can be approximated over the frequency range of interest to first order by a modified power-law with a spatial curvature as a function of frequency (Kogut 2012). This spectral smoothness can be used to separate the HI signal from foreground signals. The most common approach is to fit a smooth function to the data in the frequency space and remove it.

Several component separation techniques have been discussed in the literature for removal of the Galactic foreground, both specific to low redshift intensity mapping and to epoch of reionisation experiments. We can classify the foreground cleaning methods into two different categories: parametric and blind methods. The parametric methods are model-dependent and consist of applying a parametric fitting to each pixel in the maps (Ansari et al. 2012). The blind methods do not require any assumption on the properties of the foregrounds and the instrument response. Examples of such methods are FASTICA (Chapman et al. 2012; Wolz et al. 2014), Correlated Component Analysis (CCA) method (Bonaldi & Brown 2014), Karhunen-Loeve Decomposition (Shaw et al. 2014), GMCA (Chapman et al. 2012), principal component analysis (PCA) and independent component analysis (ICA) (Alonso et al. 2015). All methods must also deal with instrumentally induced effects such as mode-mixing of angular and frequency fluctuations induced by the dependence of the beam with frequency. The component separation methods are based on the spectral smoothness of the foregrounds, so the calibration will be a critical step in order not to compromise this smoothness.

There are two instrumental approaches to HI mapping, either using single dishes with multiple feeds or interferometer arrays. The single-dish approach offers a relatively cheap and simple way for doing intensity mapping. Unlike single-dish experiments which naturally have good surface brightness sensitivity, interferometer arrays suitable for intensity mapping will require many close-packed elements in order to detect the very low surface brightness HI signal and thus need big correlators (Thompson, Moran & Swenson 2008). Both kinds of experiment will have to deal with potential systematics similar to those encountered in cosmic microwave background (CMB) imaging experiments, such as gain variations, spillover, ground pickup and correlated noise in frequency. Single-dish experiments will require stable receiver sys-

tems, good calibration and an appropriate scanning strategy. On the other hand, interferometers are known to deal more naturally with systematics and with foregrounds than single dishes and hence receiver stability (e.g. Dickinson et al. 2004; Readhead et al. 2004), etc. is not such an important issue. However, we point out that existing interferometers are limited by the small number of their smallest baselines and hence fail to provide the required surface brightness sensitivity (Bull et al. 2015).

In this paper, we focus on the concept of a single-dish experiment with the BINGO (BAO from Integrated Neutral gas Observations) instrument, which aims at mapping the HI emission at frequencies from 960 to 1260 MHz ($z = 0.12 - 0.48$). This experiment will measure the HI power spectrum, and will detect for the first time the Baryon Acoustic Oscillations around 1 GHz. Some of the details of the BINGO experiment can be found in Battye et al. (2013). Though we use the BINGO instrument as a concrete example, nearly all the following analysis concepts can be applied to other single-dish instruments.

We organise the paper as follows. In Section 2, we describe our simulations in which we incorporate foreground and instrumental noise models. We also make some predictions of the total atmospheric contribution to the instrumental noise level and of the atmospheric fluctuations coming from the inhomogeneous distribution of water vapour. In Section 3, we focus on two simple foreground and noise subtraction procedures: parametric fitting and principal component analysis. The success of these methods depends on the smoothness of the frequency spectrum of the noise and the foreground. In Section 4, we place some requirements on the smoothness of these spectra needed for extracting the HI signal from the instrumental $1/f$ noise and from the brighter foreground, the synchrotron emission. In this way, we assess the robustness of the cleaning methods, according to the smoothness of the frequency spectrum of the simulated data.

2 SIMULATION OF A SINGLE-DISH EXPERIMENT

In order to explore the foreground cleaning methods we use simulations of the proposed BINGO telescope (Battye et al. 2013) as a concrete example of a single-dish instrument. To do this we require simulated maps of the sky at the observation frequencies. We produce a time-ordered data stream with a foreground model which includes Galactic synchrotron plus a background of unresolved point sources, detailed in Section 2.1, while the way we produce the HI signal is described in Section 2.2. In Section 2.3, we introduce the map-making method used to obtain the sky maps of the experiment and describe the instrumental noise model ($1/f$ and thermal noise) in Section 2.4. Finally, in Section 2.5, we make some predictions of the amplitude of the atmospheric noise.

2.1 Foreground model

2.1.1 Galactic synchrotron

To generate a template of the sky emission, we use the reprocessed 408 MHz Haslam et al. map (Remazeilles et al. 2014), which constitutes a good tracer of the diffuse synchrotron emission. The synchrotron spectrum in terms of brightness temperature can be approximated by $T(\nu) \propto \nu^{\beta+C \ln(\nu/\nu_0)}$ (Kogut 2012), where ν is the radiation frequency, C the curvature defined with respect to a reference frequency ν_0 and β is the spectral index at $\nu = \nu_0$. Observations have indicated that there are spatial variations of the spec-

Table 1. Summary of the different models of the Galactic synchrotron emission.

Synchrotron	Characteristics	Mean β	r.m.s. β
Model 1	β constant on the sky	-2.8	β constant
Model 2	A Gaussian spatial distribution of β	-2.8	0.17
Model 3	de Oliveira-Costa et al. (2008) model	-2.5	0.03

tral index (Reich & Reich 1988; Platania et al. 1998; Davies et al. 2006). We extrapolate this template to the frequencies of interest by using 3 different models for β listed below, from the simplest to the more complicated ones:

1. We ignore any variation across the sky of the spectral index β , we fix this index to an average value estimated at frequencies near ~ 1 GHz $\beta = -2.8$ (Platania et al. 1998).
2. We assume a Gaussian spatial distribution of the synchrotron index β , with $\langle \beta \rangle = -2.8$ and a r.m.s. value of 0.17 (Platania et al. 1998).
3. We use spectral model of the global sky from 10 MHz to 100 GHz developed by de Oliveira-Costa et al. (2008). This final model is the most realistic one. It includes spatial correlations of the Galactic emission across the sky and a frequency curvature modification of the synchrotron index β . The mean value of β is -2.5 and the steepening of this index is 0.03.

The models listed above are summarised in Table 1.

A high-resolution template of synchrotron emission is required to make realistic tests of foreground removal methods. However, the resulting synchrotron map has a resolution corresponding to a beam with FWHM equal to 56 arcmin. We require a higher resolution map so it cannot be directly used as a template of the synchrotron emission. And, there are no other full-sky astronomical data sets with resolution better than $\sim 1^\circ$. Hence, to account for these small-scale fluctuations, we add to the original map a random Gaussian realisation with a power spectrum $C_\ell = \ell^\gamma (\exp(-\ell^2 \sigma_{\text{sim}}^2))$, where $\gamma = -2.7$, σ_{sim} is the Gaussian width of the simulation and ℓ the multipole. The details are given in Miville-Deschênes et al. 2007 and Remazeilles et al. 2014.

2.1.2 Extragalactic point sources

We assume that the distribution of such sources is not spatially correlated, that is to say the clustering is weak (Liu, Tegmark & Zaldarriaga 2009) and hence that they are Poisson distributed. The clustering part increases the pixel-pixel correlations (Battye et al. 2013) and thus can have an impact on the foreground removal method. In subsequent work, we will investigate this contribution. Extragalactic point sources can be divided into two populations. The first component comprises bright and isolated point sources that can be readily detected by the instrument and removed directly using the data of the experiment. The second population consists of a continuum of unresolved sources.

At radio frequencies (GHz), the r.m.s. confusion σ_c in a telescope beam with the full width at half maximum θ_{FWHM} can be approximated by (Condon 1974)

$$\frac{\sigma_c}{\text{mJy}} \approx 0.2 \left(\frac{\nu}{\text{GHz}} \right)^{-0.7} \left(\frac{\theta_{\text{FWHM}}}{\text{arcmin}} \right)^2. \quad (1)$$

For the BINGO telescope, with a $\theta_{\text{FWHM}} = 40$ arcmin, this is around 320 mJy at 1000 MHz, thus BINGO will be subject to con-

fusion noise when considering a continuum detection. This is irrelevant for an HI line signal.

The brightness of each source is drawn from the differential source counts $\frac{dN}{dS}$, with the number of sources per steradian N and per unit of flux S . In Battye et al. (2013), they use data from multiple continuum surveys at 1.4 GHz (Mitchell & Condon 1985; White et al. 1997; Ciliegi et al. 1999; Gruppioni et al. 1999; Hopkins et al. 1999; Richards 2000; Bondi et al. 2003; Fomalont et al. 2006; Owen & Morrison 2008; Seymour et al. 2008; Ibar et al. 2010) and fit a 5th order polynomial to these data

$$\log_{10} \left(\frac{S^{2.5} dN/dS}{N_0} \right) = \sum_{i=0}^5 a_i \left[\log_{10} \left(\frac{S}{S_0} \right) \right]^i, \quad (2)$$

where $a_0 = 2.593$, $a_1 = 9.333 \times 10^{-2}$, $a_2 = -4.839 \times 10^{-4}$, $a_3 = 2.488 \times 10^{-1}$, $a_4 = 8.995 \times 10^{-2}$ and $a_5 = 8.506 \times 10^{-3}$; and $N_0 = 1 \text{ Jy}^{3/2} \text{ sr}^{-1}$ and $S_0 = 1 \text{ Jy}$. The power-law spectral function with a Gaussian distributed index is given by

$$S(\nu) = S(1.4 \text{ GHz}) \left(\frac{\nu}{1.4 \text{ GHz}} \right)^{-\alpha}. \quad (3)$$

The spectral index α is randomly chosen from a Gaussian distribution

$$P(\alpha) = \frac{1}{\sqrt{(2\pi\sigma^2)}} \exp \left[-\frac{(\alpha - \alpha_0)^2}{2\sigma^2} \right], \quad (4)$$

with a mean of $\alpha_0 = 2.5$ and a width distribution of $\sigma = 0.5$ (Tegmark et al. 2000).

Assuming that the sources with flux $S > S_{\text{max}}$ can be subtracted from the data, we estimate the mean brightness temperature, contributed due to the remaining sources, by

$$T_{\text{ps}}(\nu, \hat{n}) = \left(\frac{dB}{dT} \right)^{-1} \Omega_{\text{pix}}^{-1} \sum_{i=1}^N S_i(\nu), \quad (5)$$

where S_i is the flux of the point source i at 1.4 GHz and Ω_{sky} the pixel size equal to 0.22 arcmin^2 . The parameter $dB/dT = 2k_B/\lambda^2$ is the conversion factor between intensity units to brightness temperature units, k_B being the Boltzmann constant, λ the wavelength of the incoming radiation and Ω_{pix} the pixel size.

We expect that the brightest sources could be removed directly from the BINGO data or could be masked using the NRAO VLA Sky-Survey (NVSS) (Condon et al. 1998), which is considered to be 99% complete at a flux density limit of 3.4 mJy. For our simulation, to be conservative, we take $S_{\text{max}} = 100 \text{ mJy}$, which corresponds to ~ 1 source per square degree. We expect to either subtract or mask most of the brightest radio sources above this flux density. We will investigate in a following paper the residual contribution due to the variability of radio sources and calibration issues.

In the following, the maps are created using the HEALPix pixelisation scheme (Górski et al. 2005). A foreground map of this simulation at 1000 MHz is given in Fig. 1. The colour bar represents the brightness temperature in mK.

2.2 HI signal

We use the CORA software (Shaw et al. 2014) to simulate the HI brightness temperature. We assume the Planck+WP+highL+BAO cosmological model given in Planck Collaboration et al. (2014). The HI brightness temperature can be written as a sum of two parts

$$T_b = \bar{T}_b(1 + \delta_{\text{HI}}), \quad (6)$$

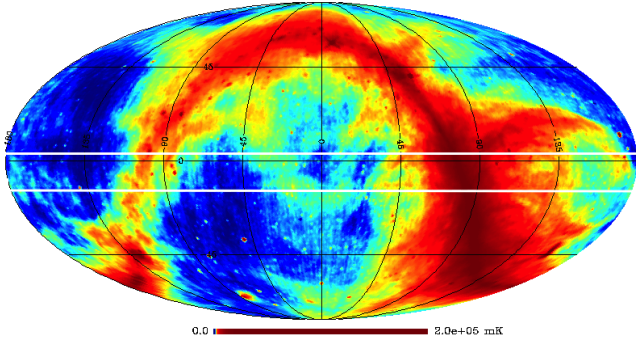


Figure 1. Mollweide projection of the foreground with a background of unresolved point sources ($S < 100$ mJy) and synchrotron emission at 1000 MHz in celestial (RA/Dec) coordinates with RA=0° at the centre and increasing to the left. The white solid lines define the spaces expected to be observed by the BINGO experiment.

where δ_{HI} is the HI density contrast and \bar{T}_b the mean HI brightness temperature given by

$$\bar{T}_b(z) = 0.3\text{K} \left(\frac{\Omega_{\text{HI}}}{10^{-3}} \right) \left(\frac{\Omega_m + (1+z)^{-3}\Omega_\Lambda}{0.29} \right)^{-1/2} \left(\frac{1+z}{2.5} \right)^{1/2}. \quad (7)$$

We assume that the neutral HI fraction is $\Omega_{\text{HI}} = 5 \times 10^{-4}$ (Switzer et al. 2013) and the HI bias is independent of scale and redshift with $b_{\text{HI}} = 1$.

The HI brightness temperature power spectrum can be modelled as

$$P_{T_b}(\vec{k}, z) = \bar{T}_b^2(z) [b_{\text{HI}} + f\mu^2]^2 D^2(z) P_m(k, z), \quad (8)$$

where $\mu \sim k_{\parallel}/k$ with the flat-sky approximation, $P_m(k, z)$ the matter power spectrum, $D(z)$ the linear growth factor normalised by $D(0) = 1$, and f the linear growth rate $f = d \log D / d \log a$, where a is the cosmological scale factor. The HI angular power spectrum is obtained from Gaussian random fields with the flat sky angular power spectrum (Datta, Choudhury & Bharadwaj 2007)

$$C_\ell^{\text{flat}}(\Delta\nu) = \frac{\bar{T}_b^2}{\pi r_v^2} \int_0^\infty dk_{\parallel} \cos(k_{\parallel} r_v \Delta\nu) P_{T_b}(\mathbf{k}), \quad (9)$$

where r_v is the comoving distance, \mathbf{k} has components k_{\parallel} and ℓ/r_v along the line-of-sight and in the plane of the sky respectively. Using these inputs, we generate the maps of the HI signal which have r.m.s. fluctuations around 0.1 mK.

2.3 Simulation of a single-dish experiment

We consider a single-dish experiment based on the BINGO concept. BINGO will be a dual mirror Compact Antenna Test Range (CATR) telescope with a 40 m primary mirror and an offset focus. Apart from the telescope optics the design of the instrument is similar to that of Battye et al. (2013). The proposed BINGO experiment will have a receiver array containing between 50 and 60 feed horns. In our simulation, we model the receiver plane with 56 feed horns with a 90 m focal length. We consider the frequency range from 960 MHz ($z = 0.48$) to 1260 MHz ($z = 0.13$). To decrease the computational speed, we choose to divide the 300 MHz band into 20 channels, each of 15 MHz bandwidth, though the actual instrument will have much narrower frequency channels to facilitate RFI excision. The sampling rate is 0.1 Hz. The instrumental parameters used for our simulation are listed in Table 2.

Table 2. Instrumental parameters for BINGO simulation.

Survey parameters	
Redshift range [$z_{\text{min}}, z_{\text{max}}$]	[0.13, 0.48]
Frequency range [$\nu_{\text{min}}, \nu_{\text{max}}$] (MHz)	[960, 1260]
Channel width $\Delta\nu$ (MHz)	15
FWHM (arcmin) at 1 GHz	40
Number of feed horns n_f	56
Sky coverage Ω_{sur} (deg ²)	3000
Observation time t_{obs} (yr)	1
System temperature T_{sys} (K)	50
Sampling rate (Hz)	0.1

We assume that the horns are arranged in a rectangular configuration spaced 3.3 m apart and the beams are given by a circular Gaussian. The beams are diffraction-limited and, therefore, the full width at half maximum θ_{FWHM} of the beam can be scaled to any frequency ν by

$$\theta_{\text{FWHM}}(\nu) = \theta_{\text{FWHM}}(\nu_0) \frac{\nu_0}{\nu}, \quad (10)$$

with $\nu_0 = 1000$ MHz and $\theta_{\text{FWHM}}(\nu_0) = 40$ arcmin.

For the following simulations, we will assume that the telescope will map a 15° declination strip centred at -5° as the sky drifts past the telescope. The declination of -5° has been chosen to minimise the foreground emission, which is lowest between 10 and -10° declination. We assume one full year of on-source integration. In practice, this will likely represent about 2 years of real observation time since we could consider only night observations we will probably remove some data due to foreseeable technical issues like such as radio frequency interference, weather downtime etc.

In order to obtain the simulated BINGO maps, we use a maximum likelihood map-making algorithm (Stompor et al. 2002; Hamilton 2003). We model the timelines \mathbf{d} as $\mathbf{d} = \mathbf{A}\mathbf{s} + \mathbf{n}$, where \mathbf{s} is the pixelized sky signal which is mapped into the timelines and corrupted by noise \mathbf{n} . The pointing information is represented by the pointing matrix \mathbf{A} of size $N_{\text{samples}} \times N_{\text{pixels}}$, which connects the time index to the pixel index. The map-making step is given by

$$\hat{\mathbf{s}} = (\mathbf{A}^T \mathbf{N}^{-1} \mathbf{A})^{-1} \mathbf{A}^T \mathbf{N}^{-1} \mathbf{d}, \quad (11)$$

where \mathbf{N} is the noise covariance matrix and $\hat{\mathbf{s}}$ is the best estimate of \mathbf{s} . An impact of the $1/f$ noise is to induce slow drifts of the gains of the receivers. If we do not take steps to mitigate it, the $1/f$ noise will introduce stripes in the maps along the direction of the drift scan. The inversion of $(\mathbf{A}^T \mathbf{N}^{-1} \mathbf{A})$ is performed by using the preconditioned conjugate gradient method. The preconditioner is a pixel domain diagonal matrix weighting the pixels by the number of times they have been observed. This method is described in detail in Cantalupo et al. (2010).

We set the HEALPix resolution of the map equal to $n_{\text{side}} = 128$, which corresponds to a map pixel size of 27 arcmin. The focal plane configuration will lead to some gaps in the observed sky band. To correct for this, we rotate the beams of the horns on the sky with an angle $\sim 5^\circ$. In Fig. 2, we show the drift scan strips of the sky emission. In the following, we consider a single frequency channel centered at 997.5 MHz to display the results. The top panel shows the HI signal and the bottom panel the Galactic synchrotron emission plus a background of unresolved point sources. The amplitude of the foreground emission is much higher than the signal of interest by four orders of magnitude (note the difference in colour-scale in the strips). These maps are plotted with a Cartesian projection using the HEALPix software.

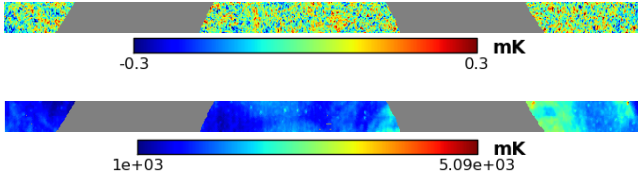


Figure 2. Two drift scan strips of the observed sky with only HI signal in the *top* panel while the bottom panel includes Galactic synchrotron emission plus a background of unresolved point sources. The mask of the Galactic plane at $|b| < 20^\circ$ is plotted with grey pixels. Note the different linear intensity scales. Colour bars represent the temperature in mK.

2.4 Instrumental noise

The timelines are corrupted by thermal (white) noise. The optimal sensitivity of the BINGO experiment per pixel can be defined as follows

$$\sigma_t = \frac{T_{\text{sys}}}{\sqrt{t_{\text{pix}} \Delta\nu}}, \quad (12)$$

where $\Delta\nu$ is the frequency channel given in Table 2. We assume the same system temperature T_{sys} for all receivers. The parameter t_{pix} is the integration time per pixel defined by

$$t_{\text{pix}} = n_f t_{\text{obs}} \frac{\Omega_{\text{pix}}}{\Omega_{\text{sur}}}, \quad (13)$$

where n_f denotes the number of feed horns, t_{obs} is the total integration time, Ω_{sur} is the survey area and Ω_{pix} is the beam area. The values of these parameters are given in Table 2. We assume $\Omega_{\text{pix}} = \theta_{\text{FWHM}}^2$ and for an integration time of one year, we obtain $\sigma_t = 25 \mu\text{K}$.

Our simulation also contains $1/f$ noise, produced by gain fluctuations of the amplifiers and thus this noise is correlated across all frequency channels. The impact of these fluctuations is usually simulated in the frequency domain using a $1/f$ power spectrum. To generate realistic $1/f$ noise we use an algorithm to create a time sequence of white noise. Then we compute its Fourier Transform and weight the data by a zero-mean power spectral density with the distribution

$$P_{\text{sd}} = \frac{\sigma_t^2}{v_{\text{samp}}} \left[1 + \left(\frac{f_{\text{knee}}}{f} \right)^\alpha \right], \quad (14)$$

where v_{samp} is the sampling frequency. f is the discrete Fourier transform sample frequency, given a length of the number of time samples and a sample spacing of $1/v_{\text{samp}}$. The $1/f$ knee value is the integration time (the inverse of the discrete Fourier transform sample frequency) at which the thermal and $1/f$ noise make equal contributions to the power spectral density. Finally, we compute the inverse Fourier transform of these data to obtain the time-ordered data of the noise.

In practice, we will filter the data on timescales of 20 min during data processing; this is the timescale for which the largest structures of interest take to drift through the BINGO field-of-view. For simplicity, we simulate each 20 min timestream separately and join them together by fixing the first sample of the n th equal to the $(n-1)$ sample. We assume the same value of the knee frequency for each receiver $f_{\text{knee}} = 10^{-3}$ Hz for a 15 MHz channel bandwidth, which corresponds to the value we aim to achieve with the BINGO pseudo-correlation receivers. The $1/f$ slope index α is assumed to be 1. In this paper, we start by making the assumption that the $1/f$ noise is perfectly correlated between the frequency channels, which is what is expected if we are dealing with simple gain fluctuations

and we assume a flat frequency spectrum ($\beta = 0$). In Section 4, we investigate what happens if these assumptions are relaxed.

In Fig. 3, we show two maps of the noise with thermal noise only (in the top panel) and with added $1/f$ noise (in the bottom panel). One can notice the stripes along the direction of the scan induced by the instrumental $1/f$ noise, which is much larger than the thermal noise by a factor of ~ 100 .

2.5 Atmospheric noise

The observations of a ground-based telescope are affected by the atmosphere at different levels, depending on the observing frequency and of course on the prevailing weather conditions. The incoming signal will be absorbed or scattered by the atmosphere. This effect increases the noise level of the instrument and we quantify this in Appendix A1. Around 1 GHz, the optical depth is dominated by oxygen which is constant in time with a small contribution from water, usually quantified in terms of the precipitable water vapour (PWV). Hence, it can undergo changes on an hourly (or faster) timescales and vary spatially. In Appendix A1 we show that the amount of PWV at 1 GHz does not have a significant impact on the total brightness temperature of the atmosphere. We find an atmospheric contribution ~ 1.81 K in days with favourable atmospheric conditions $\text{PWV} < 2$ mm, and ~ 1.82 K in days with unfavourable weather $\text{PWV} > 4$ mm. Thus, we expect the atmospheric contribution to the system temperature to be at the level of a few percent.

However, we are also concerned with the fluctuating part of the emission and absorption, which leads to an additional $1/f$ noise-like component in the time-ordered data. We quantify this effect in Appendix A2. The main source of fluctuations is atmospheric turbulence in the troposphere. Oxygen molecules are uniformly mixed in the atmosphere, but the water vapour molecules show inhomogeneities. Even if the water contributes a small percentage to the noise level, around 1%, its variations with time can produce fluctuations that are large compared to the HI signal and thermal noise. This can generate some correlations between the time streams of data from different receivers and for the same receiver at different times. These fluctuations depend on the weather conditions at the observing site, on the telescope, on the frequency bands and on the observing strategy (Church 1995; Lay & Halverson 2000). The effects of atmospheric noise have been well studied in cosmic microwave background experiments (e.g. Davies et al. 1996; Sayers et al. 2010), and can be approximated by $1/f$ noise at low-frequency. However, the amplitude of the atmospheric fluctuations in the time streams has not been measured at 1 GHz. From the back-of-the-envelope calculation detailed in Appendix A2, we find that the amplitude of the atmospheric fluctuations in antenna temperature for a single dish is $\Delta T_{\text{atm}} \sim 0.01$ mK. Thus, the amplitude of these fluctuations is below the instrumental noise, which is expected to be ~ 1 mK for a frequency resolution of 15 MHz for BINGO. So, the contribution from the atmospheric fluctuations appears not to be a challenge for a single-dish experiment observing around 1 GHz when the weather is stable.

3 FOREGROUND AND INSTRUMENTAL NOISE SUBTRACTION

For an observing frequency around 1 GHz, the synchrotron emission and the extragalactic point sources are the most relevant foregrounds. The removal of the foregrounds and instrumental $1/f$ will rely on the smoothness of their frequency spectra. In this section,

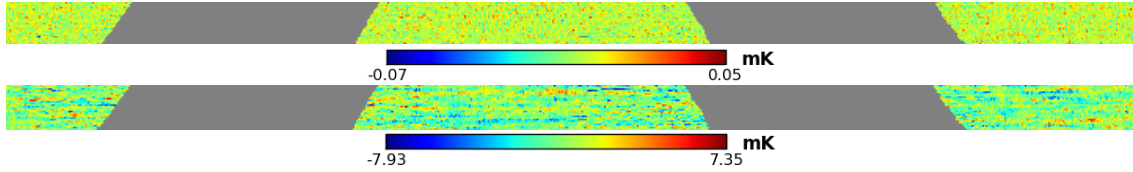


Figure 3. Maps of the drift scan of the instrumental noise. The *top* panel represents the thermal noise and the *bottom* panel the $1/f$ noise. Note the different intensity scales. Colour bars represent the temperature in mK.

we want to quantify how well the foregrounds can be subtracted in the presence of thermal and $1/f$ noise. Our philosophy is to focus on two simple cleaning procedures, parametric fitting and a blind method with principal component analysis (PCA). We describe these methods in Section 3.1 and present their results in Section 3.3. We also demonstrate the possibility of using a blind method to remove the instrumental $1/f$ noise in Section 3.2. In the following, we assume no systematics and a perfect calibration of the data.

3.1 Methods

3.1.1 Parametric fitting

Parametric fitting is a common method to parameterise foregrounds (e.g. Brandt et al. 1994; Ansari et al. 2012). The approach of the method is to fit directly an explicit parametric model of the foregrounds and noise to each pixel of the maps along the frequency direction. The common foreground model is a modified power-law. As the main foreground emission, the Galactic synchrotron can be approximated by a parametric distribution with a curvature to first order (Kogut 2012).

The i -th pixel of the simulated map of the sky at the frequency ν_j can be written as the sum of the intensity of the HI signal $T_{21\text{cm}}^i$, the foreground emissions T_{fg}^i and the noise of the instrument T_{n}^i

$$\hat{T}_j^i = \hat{T}_{21\text{cm},j}^i + \hat{T}_{\text{fg},j}^i + \hat{T}_{\text{n},j}^i. \quad (15)$$

The hat symbol denotes a modelled quantity. We make the assumption that the foreground \hat{T}_{fg} and $1/f$ noise \hat{T}_{n} can be modelled by

$$\hat{T}_{\text{fg},j}^i + \hat{T}_{\text{n},j}^i = A^i \left(\frac{\nu}{\nu_0} \right)^\beta, \quad (16)$$

where β is the spectral index and A is the amplitude in mK. This assumption on the spectral slope of the $1/f$ noise can be justified by the fact that the $1/f$ noise fluctuations are expected to have a spectral form similar to the system temperature, which can be approximated by a power-law over the BINGO frequency range. We fit Eq. 16 for each pixel of the map in the frequency direction minimised using a least-squares method.

3.1.2 Principal Component Analysis (PCA)

PCA (Murtagh & Heck 1987) has the advantage of being a non-parametric method and so requires no specific prior information on the spectra of the foreground and the noise. This method consists of transforming the independent maps of each frequency channel into orthogonal modes according to the covariance between frequencies. We consider the data to be a matrix S , with $N_f \times N_p$ elements. N_f denotes the number of frequency channels and N_p the number of pixels in the map. We compute the frequency covariance matrix from the simulated data

$$C_{ij} = \frac{1}{N_p} S S^T = \frac{1}{N_p} \sum_{p=1}^{N_p} T(\nu_i, \hat{n}_p) T(\nu_j, \hat{n}_p), \quad (17)$$

where $T(\nu_i, \hat{n}_p)$ is the brightness temperature along the direction of the line-of-sight \hat{n}_p and for the frequency channel ν_i . Therefore, we can compute the entries of the correlation matrix between each pair of frequency channels

$$R_{jk} = \frac{C_{jk}}{C_{jj}^{1/2} C_{kk}^{1/2}}, \quad (18)$$

where the indices run from 1 to N_f . We diagonalise the correlation matrix of the full data set with an eigenvalue decomposition and obtain

$$P^T R P = \Lambda \equiv \text{diag} \{ \lambda_1, \dots, \lambda_{N_f} \}, \quad (19)$$

where the diagonal elements of the matrix Λ are the eigenvalues λ_j of the matrix R and the matrix P is an orthogonal matrix which contains the eigenvectors. The variance of each mode is given by the amplitude of the eigenvalues λ_j , so each eigenvalue measures the contribution of its corresponding eigenvector to the total sky variance.

This method parameterises the foreground and noise components and produces independent eigenfunctions, which convert the spectral correlation into a number of largest variance modes. We pick the eigenvalues with the correlated components in frequency with the larger variances. So, we build a matrix P_c , with only the corresponding eigenvectors and we use this matrix to decompose the data into eigenfunctions ϕ

$$\phi = P_c^T S. \quad (20)$$

The maps S_c of the reconstructed foreground and $1/f$ noise are obtained by transforming back to the frequency space

$$S_c = P_c \phi. \quad (21)$$

Finally, we find the maps of the reconstructed HI signal S_{HI} by subtracting the input maps and the reconstructed foreground and $1/f$ noise

$$S_{\text{HI}} = S - S_c. \quad (22)$$

3.2 $1/f$ noise subtraction using PCA

First, we apply the PCA method to thermal and $1/f$ noise components only, ignoring foregrounds for the moment. The frequency spectrum of the correlated noise ($1/f$) is also expected to be smooth in frequency. Thus, one can use the PCA method to remove the instrumental $1/f$ noise. We show the result in Section 3.2.1 and we test the robustness of this noise removal method with different models of the $1/f$ noise in Section 3.2.2.

3.2.1 PCA results

The instrumental noise is simulated as explained in Section 2.4, and we apply the PCA method to the maps of the instrumental noise. The $1/f$ noise is computed with the knee frequency $f_{\text{knee}} = 1$ mHz, which is thought to be achievable using balanced correlator receivers (Jarosik et al. 2003; Bersanelli et al. 2010). Note that a different scanning strategy than a drift-scan strategy can remove the $1/f$ noise in the map-making, but for a transit telescope, such as BINGO, we will rely on component separation and the smoothness of the frequency spectrum. In the top panel of Fig. 4 we plot the power spectra of the noise maps with different number of modes removed: 1, 2 and 3. The spectra of the maps are computed to $\ell < 1000$ using PolSpice (Szapudi, Prunet & Colombi 2001; Chon et al. 2004; Challinor & Chon 2005). This code computes correlation functions and estimates the power spectra by integrating the resampled correlation function using Legendre-Gauss integration. The power spectra are corrected for the effect of the cut sky and for the beam and pixel window functions. In order to remove the ringing in the power spectra, we apodize the correlation function with a Gaussian of width 15° . Subtracting one mode does not remove the $1/f$ noise sufficiently well, but the thermal noise level can be reached by removing 2 modes as displayed in Fig. 4. This plot shows the residuals between the recovered thermal noise and the input thermal noise. For the case of two removed modes, the residual is significantly lower than the input thermal noise at all scales. It shows that we can recover the thermal noise model sufficiently well using principal component analysis by subtracting at least 2 principal modes.

3.2.2 Results with different noise models

In order to test the efficiency of the PCA method, we compute the instrumental noise with different values of the knee frequency f_{knee} between 1 mHz and 10 Hz. Note that a knee frequency of 1 mHz might be expected for a pseudo-correlation receiver and that 10 Hz is a worst-case scenario for a single channel radiometer. We find that the residual noise after removing 2 principal modes is independent of the input knee frequency and, hence, the PCA method is robust. We emphasise that we have assumed a flat frequency spectrum for the $1/f$ noise (i.e. it affects all frequency channels equally). The efficiency of the noise cleaning method depends on this assumption and on assuming a perfect calibration. We will quantify the success of this method as the function of the smoothness of the $1/f$ noise in Section 4.

3.3 Inclusion of foreground emission

In this Section, we show the results for the detection of the HI signal from the total intensity maps in the presence of instrumental noise and foreground emission, using the parametric fitting and principal component analysis methods. We compare both methods in Section 3.3.1 and we focus on the results of the principal component analysis method in Section 3.3.2. We look at the residuals of the reconstructed cosmological signal in Section 3.3.3.

3.3.1 Parametric fitting results

Here we present the results of the parametric fitting method. The extraction of the HI signal is done using only the frequency information. The fit is made for each pixel. In Fig. 5, we show the measurements as a function of frequency, for a random line-of-sight,

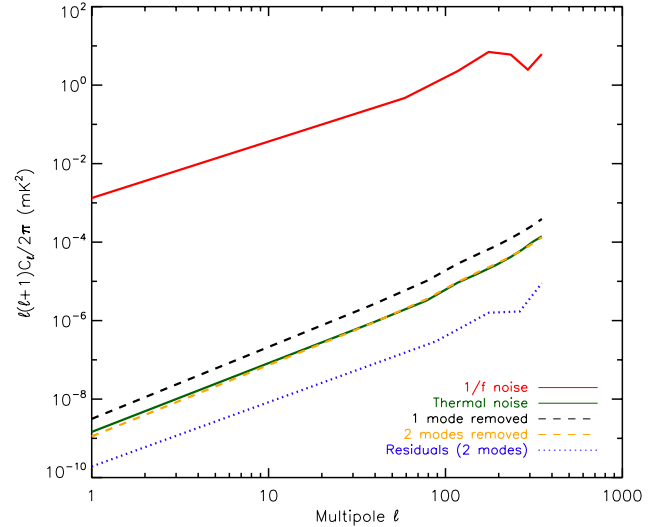


Figure 4. Power spectra of the simulated noise maps after applying principal component analysis. We show the input $1/f$ noise (red solid line) and the input thermal noise (green solid line), the reconstructed noise after applying principal component analysis with 1 mode removed (black dashed line) and with 2 modes removed (orange dashed line). We display the power spectrum of the difference between the maps of the input thermal noise and of the reconstructed thermal noise after PCA with 2 modes removed (blue dotted line). It is below the input thermal noise at all scales.

with the synchrotron model 3 quantified in Table 1 and a background of unresolved point sources ($S < 100$ mJy) as explained in Section 2.1.2. The result is averaged over 20 realisations of the instrumental noise (thermal and $1/f$ noise). The top panel represents the simulated measurements and the reconstructed foreground emission with parametric fitting, highlighting the smooth component of the foreground. The bottom panel represents the recovered cosmological signal with parametric fitting and principal component analysis after removing 7 modes compared to the input one. It shows that the parametric fitting, while superficially in agreement with the input signal, does not provide an accurate fit to the signal of interest compared to the PCA method.

3.3.2 Results of PCA applied to sky maps

Fig. 5 shows that PCA induces a small offset in the reconstructed HI signal: some cosmological signal leaks into the reconstructed foreground and noise components. However, with this method, the HI signal is well recovered with a relative error of $\sim 7\%$.

Here we will quantify the impact of the foreground residuals on the reconstructed HI signal after applying the PCA method to the simulated sky maps. In order to check the effectiveness of the foreground removal method, we define the relative error by

$$|T_{\text{HI}}(\nu) - \hat{T}_{\text{HI}}(\nu)|/\sigma_n, \quad (23)$$

where $T_{\text{HI}}(\nu)$ is the true HI signal at frequency ν , $\hat{T}_{\text{HI}}(\nu)$ the recovered signal, and σ_n the standard deviation of the thermal noise. Fig. 6 represents the relative error as a function of the number of subtracted modes for a simulation with HI signal, $1/f$ and thermal noise and different models of foreground. We apply the PCA technique to each of the foreground models discussed in Section 2.1.1.

Since the foreground and the $1/f$ noise spectra do not contain sharp features, we can expect that they are well described by a

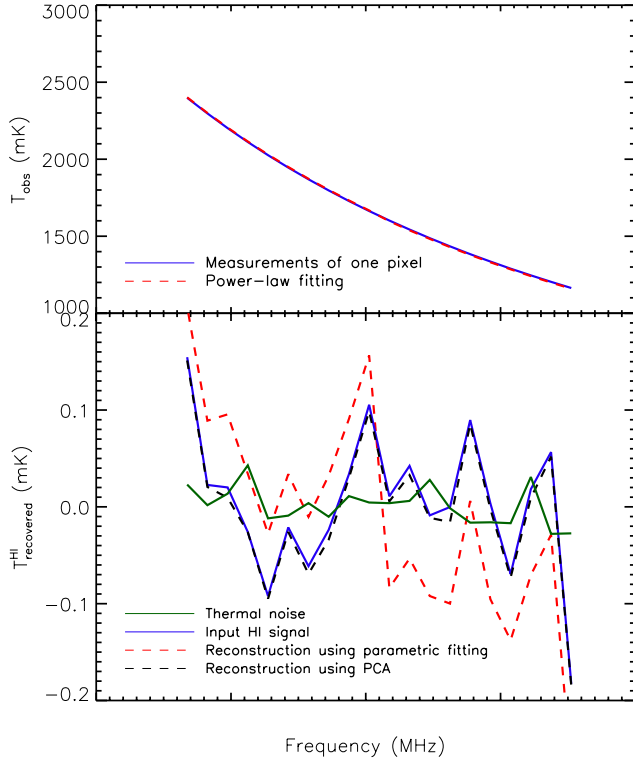


Figure 5. *Top panel:* brightness temperature of one particular line-of-sight as a function of frequency composed of sky emissions and instrumental noise (blue solid line), averaged over 20 realisations and the fit based on a parametric fitting (red dashed line). *Bottom panel:* the recovered HI signal from parametric fitting (red dashed line) and from principal component analysis (black dashed line). We show the input HI (blue solid line) and the thermal noise (green solid line).

small number of eigenvectors, so the eigenvalues are much larger for the first few principal components. This implies that a small number of components contains almost all of the foreground emission and the $1/f$ noise. Fig. 6 shows a fall-off of the amplitude of the eigenvalues with an increase in the value of the number of principal components. This steep drop means that the spectra are dominated by relatively few components, which are related to the foreground and smooth instrumental contamination. Furthermore, this figure shows that the foreground model has an impact on the extraction of the HI signal as the most complex foreground model (model 3) requires more modes to be removed in order to subtract the same level of foreground contamination. With the same noise model, the first foreground model requires the removal of at least 3 principal modes, the second model, 4 modes and the third model, 7 modes.

We notice that, when a larger number of modes is removed beyond a certain threshold, the relative error associated with each foreground model begins to increase. This can be understood in terms of the component separation method inducing a leakage of the cosmological signal in the foreground eigenvectors. This becomes even more important when we remove a larger number of principal modes from the initial maps. For the most realistic foreground model, model 3, the cosmological signal is well recovered with a relative error of $\sim 7\%$ after subtracting 7 modes and the percentage error increases to $\sim 9.5\%$ with 11 modes removed.

To evaluate the performance of the PCA method, we calculate

the amount of leakage of the HI signal into the subtracted modes using Eq. 20. The relation between the maps of the HI signal at each frequency channel S_{HI} and the orthogonal matrix P which contains the principal modes of the maps is given by the eigenfunctions ϕ

$$\phi = P^T S_{\text{HI}}. \quad (24)$$

Finally, we obtain the maps of the leakage of the HI signal S'_{HI} using the orthogonal matrix P_c , which contains only the eigenvectors removed from the initial maps

$$S'_{\text{HI}} = P_c \phi. \quad (25)$$

Removing 7 principal modes with the PCA method enables one to recover the HI signal. However, this induces a loss of the cosmological signal of $\sim 5\%$. In order to determine the foreground component that has the most impact on the foreground separation, we generate maps of the sky emission with only synchrotron emission and HI signal, and maps with a background of unresolved point sources and HI signal. The maps with synchrotron emission require the removal of 3 modes in order to extract the signal of interest, and we obtain a leakage of the HI signal in the removed principal modes of $\sim 2.4\%$. To recover the HI signal from maps with only a background of unresolved point sources, the subtraction of 1 mode is required and leads to a leakage of $\sim 1.6\%$ of the cosmological signal. Subtracting too many principal modes induces a significant loss of the cosmological signal, while when an insufficient number of modes is removed, the recovered HI signal will be still affected by the foreground contamination.

Up to now we have assumed a perfect smoothness of the foreground spectra. This assumption could be broken in the presence of instrumental systematic effects such as not sufficient knowledge of the beams, imperfect polarisation purity and mis-calibration will affect the results of the component separation methods, adding additional uncertainties. To measure the BAO wiggles from the HI power spectrum, we require that the statistical error dominates the errors from foreground cleaning methods and calibration. For the present analysis, we neglect calibration systematics, postponing discussion of the required calibration accuracy needs to be done to a future paper. We are however aware that accurate calibration of bandpasses and beam polar diagrams is essential. Quantifying calibration requirements will be done with an end-to-end pipeline. We are also investigating a more complex foreground cleaning method, which uses combined spatial and spectral filtering techniques based on the expertise from the CMB (e.g. Leach et al. 2008; Remazeilles, Delabrouille & Cardoso 2011 and Olivari et al. in prep.).

3.3.3 Maps of the reconstructed HI signal and power spectra

We perform the foreground cleaning using the PCA method with 7 modes subtracted and the parametric fitting. In Fig. 7, we display the maps of the recovered HI signal for the foreground model 3. The simulations contain instrumental noise ($1/f$ and thermal noise). To compare with the results of the cleaning methods, we plot in the first strip the true HI signal. The second, third and fourth strips show the reconstructed HI signal after 1, 3 and 7 principal modes are removed respectively. One can notice the similarity between the reconstructed HI signal shown in the fourth strip and the strip of the true HI signal. These two maps show that we can extract the cosmological signal from a highly contaminated map. The fifth strip represents the recovered HI signal after applying parametric fitting. Noting that the temperature scales are different, we observe significant differences between the input HI strip and that recovered

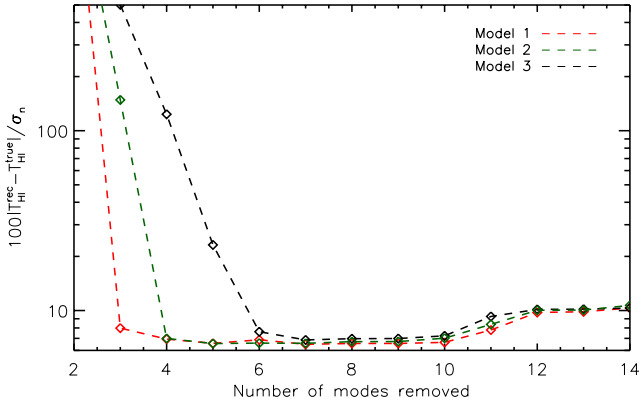


Figure 6. The percentage relative error of the thermal noise as a function of the number of modes removed. We plot the error for a foreground model with a background of unresolved point sources and Galactic synchrotron emission with a constant index $\beta = -2.8$ (red dashed line), with the introduction of the random spatial distribution of the index β across the sky (green dashed line), and with correlated spatial and spectral variations of the index β plus a background of unresolved point sources (black dashed line). These models correspond respectively to models 1, 2 and 3 explained in Table 1. The relative error increases significantly above 10 modes due to the leakage of the cosmological signal into the reconstructed foreground and correlated noise components.

with parametric fitting. It is clear that parametric fitting does not provide a sufficiently good fit to foreground and noise components.

It is evident that parametric fitting does not remove the foreground completely, thus resulting in foreground leaking into the reconstructed cosmological signal. To highlight the comparison between parametric fitting and PCA, we show in Fig. 8 the dispersion, pixel by pixel, between the recovered HI signal as a function of the input HI signal, obtained from parametric fitting and from PCA. This plot shows that parametric fitting is much less effective than the PCA method and induces a bias in the reconstructed HI signal.

We can quantify the leakage of the thermal noise and of the cosmological signal into the reconstructed foreground and noise components by calculating their power spectra and comparing them to their input power spectra. In the bottom panel of Fig. 9, we display the power spectra of the true and the recovered HI signal after the removal of 7 modes. This figure shows that both parametric fitting and PCA methods remove several orders of magnitude of foreground contamination and $1/f$ noise, but PCA gives lower residuals than the parametric fitting method. We plot the cosmological signal leakage into the foreground and $1/f$ noise reconstruction in the bottom panel. The power spectra of the thermal noise leakage and the HI signal leakage are lower than the input HI signal at all scales, thus, with PCA, it is feasible to extract the HI signal from a highly contaminated foreground map.

4 REQUIREMENTS ON FOREGROUND AND INSTRUMENTAL NOISE FREQUENCY SPECTRA

For almost all component separation techniques developed for intensity mapping data analysis, the efficiency of these methods depends on the spectral smoothness of the foreground and that of the $1/f$ noise and the bandpass calibration. We are confident that the foregrounds have sufficiently smooth spectra in frequency. This characteristic enables us to remove the components correlated in

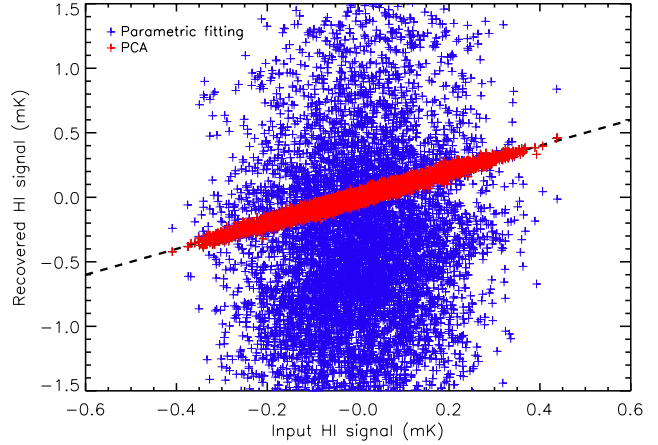


Figure 8. Scatter plot of the recovered HI signal from parametric fitting (blue markers) and from principal component analysis (red markers) as a function of the input HI signal. The parametric fitting is more noisy than the principal component analysis and also appears to be biased. The black dashed line represents the perfect correlation between the recovered HI signal and the true signal.

frequency and, therefore, to recover the HI signal with the instrumental white noise. However, some structure in the receiver band-passes is inevitable caused by amongst other things, standing waves, frequency variations in the receiver gain temperature and spectrally dependent beam patterns. The effect of these can all be reduced by careful calibration but it is important to know how good this calibration has to be. In this section we define some requirements on the smoothness of the instrumental bandpass. In the following, for the foreground emission, we consider only the brightest component; i.e. the Galactic synchrotron emission.

To quantify the effect of a non-smooth bandpass, we add to the measured frequency spectrum a sinusoidal wave defined by

$$\phi(\nu) = A \sin\left(\frac{\pi\nu}{\Delta\nu}\right), \quad (26)$$

where A is the amplitude, ν the frequency of observation and $\Delta\nu$ the wavelength. We explore a range of A between 1 and 150 mK and a range of $\Delta\nu$ between 1 to 300 MHz.

We show the modified spectra for different values of A and $\Delta\nu$ in Fig. 10. To highlight the impact of the addition of the sinusoidal wave, we divide the resulting spectrum by the original one. We see curvature and/or oscillations in the resulting spectra. A higher value of $\Delta\nu$ leads to a curvature of the spectrum, similar to a standing wave, whereas a smaller value induces a sinusoidal wave that behaves in a similar way to noise, when $\Delta\nu$ is smaller than the frequency channel width.

In what follows, we simulate the maps generated by the instrument with the same model of the Galactic synchrotron emission, HI signal and instrumental noise (thermal and $1/f$ noise) and we add Eq. 26 the sinusoidal wave to the frequency spectrum of the generated data. In order to extract the signal of interest, we apply the principal component analysis to the maps. In Fig. 11, we plot the relative error of the recovered HI signal as a function of the amplitude A and $\Delta\nu$ after applying PCA with 6 modes subtracted. The colour bar represents the amplitude of the relative error between the recovered HI signal and the true signal. The smoothness of the frequency spectrum, i.e. the value of $\Delta\nu$, has a significant impact on the efficiency of the cleaning methods. The relative error increases with a small value of $\Delta\nu$, which corresponds to a sinusoidal wave

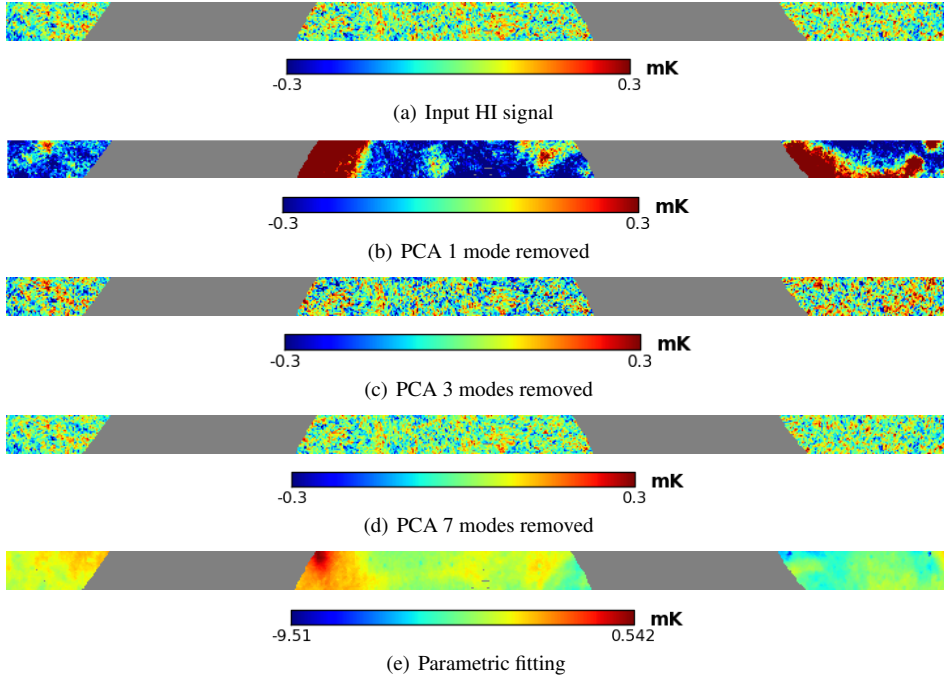


Figure 7. Five versions of a strip in declination of the HI signal. The input cosmological signal is shown in the first strip and the reconstructed signal from principal component analysis in strips 2, 3 and 4 (after 1, 3 and 7 modes removed respectively) and from parametric fitting in strip 5. Notice the different colour bar scales.

with a period shorter than the frequency channel width. In order not to be affected by the variation of the bandpass, the value of $\Delta\nu$ has to be lower than 100 MHz and the amplitude A has to be below 45 mK. With the values $A < 40$ mK and $\Delta\nu < 100$ MHz, we find a relative error $< 7.3\%$ after 6 modes are subtracted with the PCA. In absolute terms, after subtracting 6 principal modes, we obtain residuals lower than 0.1 mK, which means that the HI signal can be detected.

Finally, we perform simulations varying the number of frequency channels used to perform the PCA. We consider 20 frequency channels (15 MHz channel bandwidth) and 200 frequency channels (1.5 MHz channel width) and we test different values of $\Delta\nu$. We choose the amplitude of the sinusoidal wave to $A = 120$ mK. Fig. 12 shows the relative error between the recovered HI signal and the input signal as a function of the smoothness of the frequency spectrum $\Delta\nu$ after removing 6 and 7 principal modes. We find that the PCA method does better with a larger number of channels. The relative error is $< 7\%$ for 6 removed modes when we have 200 frequency channels for all values of $\Delta\nu$ between 1 to 400 MHz. The reason for the improvement when more channels are added can be understood by the fact that the frequency band is better sampled. Thus, as long as we have a frequency spectrum with slow oscillations, or enough frequency channels to sample the spectrum with sufficient accuracy, the smoothness of the bandpass does not constitute an issue for the foreground and the $1/f$ noise cleaning methods. An amplitude around 40 mK requires the bandpass to be calibrated to an accuracy of better than 1 part in 1000. However, one would expect to calibrate at least every day so we will only require a dynamic range of 1 part in 50.

5 CONCLUSION

In Section 2, we have simulated the kind of data which would be produced in a single-dish intensity mapping experiment like BINGO. We have adopted a sky model with Galactic synchrotron emission and a background of point sources (< 10 mJy). We have added both white and $1/f$ noise. This simulation can be generalised to any intensity mapping experiment with a drift scan strategy. This work has yielded several results concerning the challenge of any future single-dish experiment in terms of foreground, atmospheric and instrumental noise.

We have made some estimates of the total amplitude of the atmospheric noise and of its fluctuations arising from turbulences in emission of the water vapour. At 1 GHz, we have found that the r.m.s. noise level induced by these fluctuations is ~ 0.01 mK below the instrumental noise level for the BINGO experiment. Thus, for an observing frequency around 1 GHz, the atmospheric contamination should not constitute a challenge for a single-dish experiment.

We have investigated the problem of cleaning foreground contamination in order to recover the HI signal. We have focused on simple methods based on the spectral information contained in the signal. We have considered two different foreground cleaning methods, a non-blind method with parametric fitting and a blind method with PCA. This last method does not require any assumption on the physics of the foreground emissions. We have shown that the parametric fitting method does not provide an accurate fit to the data for a simulation with instrumental noise and foreground emissions. In contrast, by subtracting 7 principal modes, with a realistic foreground model, PCA enables to reach the HI signal level. Thus, on simulated data, the application of the PCA method shows that it is feasible to extract the cosmological signal across a wide range of multipoles and redshifts.

However, we have found that PCA induces a small offset in the reconstructed the HI signal of $\sim 5\%$. This result is confirmed by

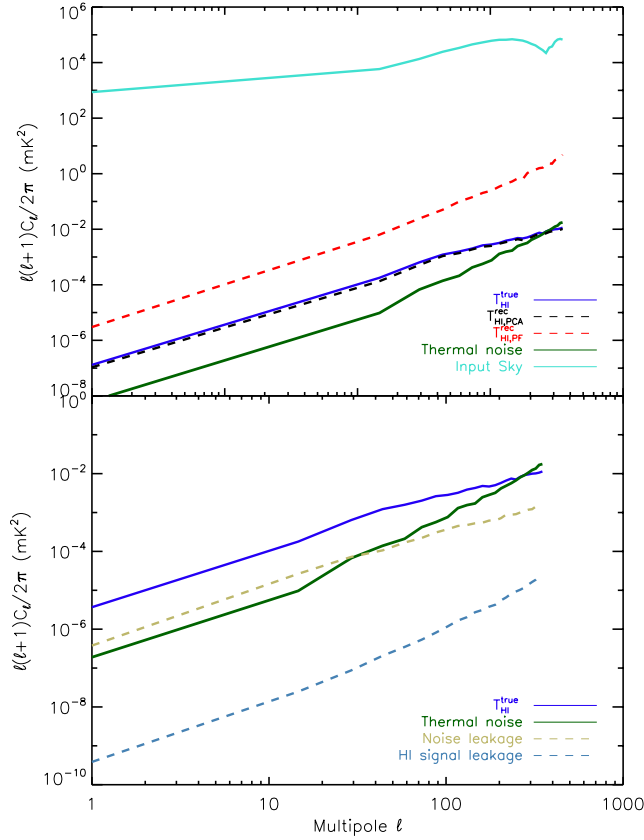


Figure 9. *Top panel:* the power spectra of the simulated maps after applying foreground cleaning. This plot shows the simulated HI signal (blue solid line), the thermal noise (green solid line) and the sky emission (cyan solid line). We plot the results of the foreground cleaning from principal component analysis (black dashed line) and from parametric fitting (red dashed line). *Bottom panel:* the power spectra of the leakage of the HI signal (dotted light blue line) and of the noise (gold dashed line) after applying PCA. The principal component analysis method clearly makes it possible to extract the HI signal.

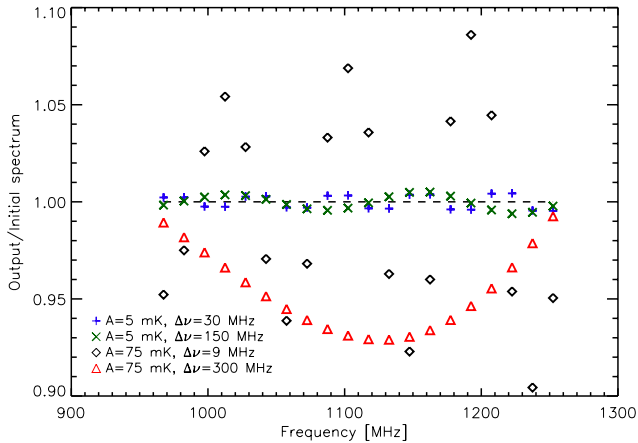


Figure 10. The corrupted spectrum divided by the original, undistorted, spectrum for different versions of the sinusoidal wave. A small value of $\Delta\nu$ induces a spectrum that fluctuates in frequency in a similar way to random noise, while a large value of $\Delta\nu$ leads to a curvature of the frequency spectrum.

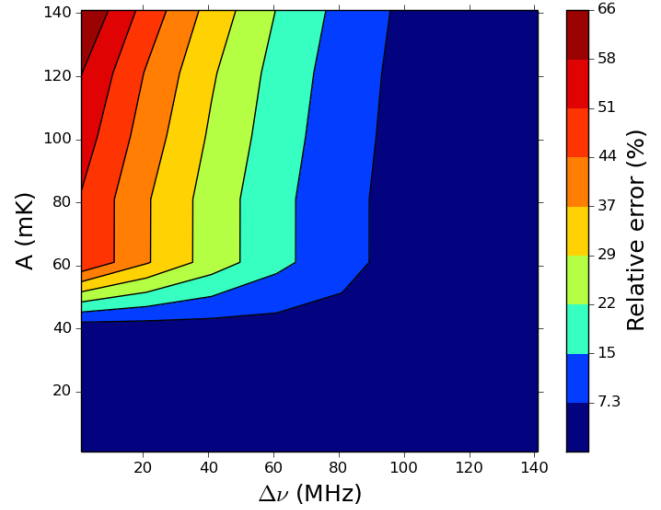


Figure 11. Relative error as a function of the amplitude A and the period $\Delta\nu$ of the sinusoidal wave after foreground and noise subtraction after applying principal component analysis (6 modes removed). The values A and $\Delta\nu$ of the sinusoidal waves are indicated on the axes of the plot. The colour bar gives the percentage error relative to the noise.

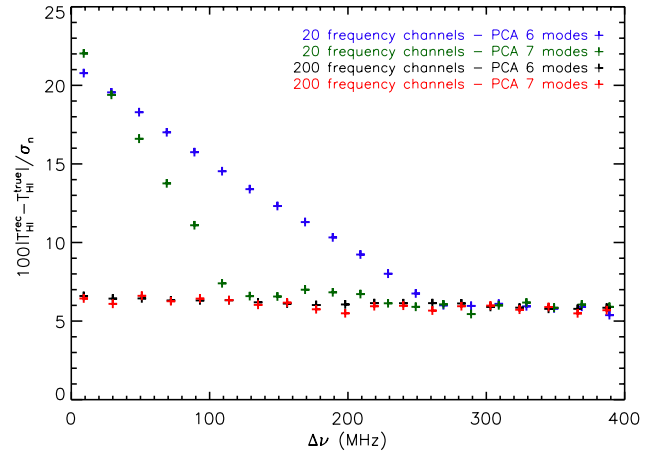


Figure 12. The percentage relative error as a function of the period $\Delta\nu$ of the sinusoidal wave after foreground removal. We show the relative errors for 20 frequency channels with 6 modes removed (blue markers), for 20 frequency channels with 7 modes removed (green markers) and for 200 frequency channels with 6 and 7 modes removed (red and black markers) respectively.

other recent works (Alonso et al. 2015), which have shown that it is possible to recover successfully HI signal from a highly contaminated foreground map with a blind method but that the foreground removal induces a bias in the HI power spectrum. In spite of this HI leakage into the removed contamination, a modification of the global shape of the power spectrum should not modify the positions of the BAOs wiggles (Wolz et al. 2014) and therefore will not have significant impact on our ability to measure the BAO scale. If the PCA method is chosen, we can correct for this small bias by calibrating it with simulations. We are also investigating a more complex cleaning method, which utilises both the spectral and spatial information (Olivari et al., in prep.), and therefore should be more accurate.

Given the assumption that the frequency spectrum of the $1/f$

noise is flat, or at least only has slow variations across the band, we have shown that PCA can cope with $1/f$ noise with relatively high knee frequencies. It is easily removed from the noise maps by subtracting 2 principal modes and the $1/f$ noise contamination is dampened down to the level of the thermal noise. This result implies that it might be possible to simplify the design of an experiment, such as BINGO, by removing the correlation receivers. In subsequent work, we plan to investigate more complex $1/f$ noise models.

The effectiveness of the blind cleaning methods depends on the spectral smoothness of the foregrounds and the instrumental $1/f$ noise. In order to challenge our cleaning methods, we have considered instrumentally distorted frequency spectra of the components we want to remove. We have shown that a sinusoidal distortion of the frequency spectrum can induce higher residuals on the maps. However, for a sinusoidal wave with an amplitude $A < 45$ mK and period $\Delta\nu < 100$ MHz, after subtracting six principal modes from the initial maps, the residuals of the noise and the sky emission are below 0.1 mK, which could enable the successful extraction of the HI signal. Still, accurate calibration will be critical for the success of measuring Baryon Acoustic Oscillations and probing the expansion history of the Universe. How good this calibration needs to be will be investigated in a future paper. The results of this paper show that the principal component analysis method is a promising tool for the extraction of the cosmological signal in any future HI intensity mapping experiment.

6 ACKNOWLEDGEMENTS

MABS, CD, MR and YZM acknowledge support from an ERC Starting Grant (no. 307209). We acknowledge use of the `HEALPix` package (Górski et al. 2005) and the python tools, `PyOperators` and `PySimulators` (Chanial & Barbey 2012). We would like to thank the BINGO collaboration for providing the basic concept for which this work was based.

REFERENCES

- Alonso D., Bull P., Ferreira P. G., Santos M. G., 2015, *MNRAS*, 447, 400
- Ansari R. et al., 2012, *A&A*, 540, A129
- Battye R. A., Browne I. W. A., Dickinson C., Heron G., Maffei B., Pourtsidou A., 2013, *MNRAS*, 434, 1239
- Battye R. A., Davies R. D., Weller J., 2004, *MNRAS*, 355, 1339
- Bersanelli M. et al., 2010, *A&A*, 520, A4
- Bonaldi A., Brown M. L., 2014, *ArXiv e-prints*
- Bondi M. et al., 2003, *A&A*, 403, 857
- Bowman J. D., Morales M. F., Hewitt J. N., 2007, *ApJ*, 661, 1
- Brandt W. N., Lawrence C. R., Readhead A. C. S., Pakianathan J. N., Fiola T. M., 1994, *ApJ*, 424, 1
- Bull P., Ferreira P. G., Patel P., Santos M. G., 2015, *ApJ*, 803, 21
- Butler B., 2002, *VLA Test Memo*, 232
- Cantalupo C. M., Borrill J. D., Jaffe A. H., Kisner T. S., Stompor R., 2010, *ApJS*, 187, 212
- Challinor A., Chon G., 2005, *MNRAS*, 360, 509
- Chang T.-C., Pen U.-L., Peterson J. B., McDonald P., 2008, *PASP*, 100, 091303
- Chanial P., Barbey N., 2012, in *SF2A-2012: Proceedings of the Annual meeting of the French Society of Astronomy and Astrophysics*, Boissier S., de Laverny P., Nardetto N., Samadi R., Valls-Gabaud D., Wozniak H., eds., pp. 513–517
- Chapman E. et al., 2012, *MNRAS*, 423, 2518
- Chon G., Challinor A., Prunet S., Hivon E., Szapudi I., 2004, *MNRAS*, 350, 914
- Church S. E., 1995, *MNRAS*, 272, 551
- Ciliegi P. et al., 1999, *MNRAS*, 302, 222
- Condon J. J., 1974, *ApJ*, 188, 279
- Condon J. J., Cotton W. D., Greisen E. W., Yin Q. F., Perley R. A., Taylor G. B., Broderick J. J., 1998, *The Astronomical Journal*, 115, 1693
- Danese L., Partridge R. B., 1989, *ApJ*, 342, 604
- Datta K. K., Choudhury T. R., Bharadwaj S., 2007, *MNRAS*, 378, 119
- Davies R. D., Dickinson C., Banday A. J., Jaffe T. R., Górski K. M., Davis R. J., 2006, *MNRAS*, 370, 1125
- Davies R. D. et al., 1996, *MNRAS*, 278, 883
- de Oliveira-Costa A., Tegmark M., Gaensler B. M., Jonas J., Landecker T. L., Reich P., 2008, *MNRAS*, 388, 247
- Dickinson C. et al., 2004, *MNRAS*, 353, 732
- Fomalont E. B., Kellermann K. I., Cowie L. L., Capak P., Barger A. J., Partridge R. B., Windhorst R. A., Richards E. A., 2006, *The Astrophysical Journal Supplement Series*, 167, 103
- Górski K. M., Hivon E., Banday A. J., Wandelt B. D., Hansen F. K., Reinecke M., Bartelmann M., 2005, *ApJ*, 622, 759
- Grupponi C. et al., 1999, *MNRAS*, 305, 297
- Hamilton J.-C., 2003, *Comptes Rendus Physique*, 4, 871, dossier: The Cosmic Microwave Background
- Hopkins A., Afonso J., Cram L., Mobasher B., 1999, *ApJ*, 519, L59
- Ibar E., Ivison R. J., Best P. N., Coppin K., Pope A., Smail I., Dunlop J. S., 2010, *MNRAS*, 401, L53
- Jarosik N. et al., 2003, *ApJS*, 148, 29
- Kogut A., 2012, *ApJ*, 753, 110
- Lay O. P., Halverson N. W., 2000, *ApJ*, 543, 787
- Leach S. M. et al., 2008, *A&A*, 491, 597
- Liu A., Tegmark M., Zaldarriaga M., 2009, *MNRAS*, 394, 1575
- Loeb A., Wyithe J. S. B., 2008, *Physical Review Letters*, 100, 161301
- Mao Y., Tegmark M., McQuinn M., Zaldarriaga M., Zahn O., 2008, *Phys. Rev. D*, 78, 023529
- Masui K. W. et al., 2013, *ApJ*, 763, L20
- McQuinn M., Zahn O., Zaldarriaga M., Hernquist L., Furlanetto S. R., 2006, *ApJ*, 653, 815
- Mitchell K. J., Condon J. J., 1985, *AJ*, 90, 1957
- Miville-Deschênes M.-A., Lagache G., Boulanger F., Puget J.-L., 2007, *A&A*, 469, 595
- Murtagh F., Heck A., 1987, *Multivariate Data Analysis*. Kluwer Academic Publishers, Boston, USA
- Owen F. N., Morrison G. E., 2008, *AJ*, 136, 1889
- Pardo J. R., Cernicharo J., Serabyn E., 2001, *IEEE Transactions on Antennas and Propagation*, 49, 1683
- Peterson J. B. et al., 2009, in *Astronomy*, Vol. 2010, astro2010: The Astronomy and Astrophysics Decadal Survey, p. 234
- Peterson J. B., Bandura K., Pen, 2006, in *Proceedings of 41st Rencontres de Moriond*
- Planck Collaboration et al., 2014, *A&A*, 571, A16
- Platania P., Bensadoun M., Bersanelli M., Amici G. D., Kogut A., Levin S., Maino D., Smoot G. F., 1998, *ApJ*, 505, 473
- Readhead A. C. S. et al., 2004, *Science*, 306, 836
- Reich P., Reich W., 1988, *A&A*, 196, 211

- Remazeilles M., Delabrouille J., Cardoso J.-F., 2011, MNRAS, 410, 2481
- Remazeilles M., Dickinson C., Banday A. J., Bigot-Sazy M.-A., Ghosh T., 2014, ArXiv e-prints (1411.3628), submitted to MNRAS
- Richards E. A., 2000, ApJ, 533, 611
- Sayers J. et al., 2010, ApJ, 708, 1674
- Seymour N. et al., 2008, MNRAS, 386, 1695
- Shaw J. R., Sigurdson K., Pen U.-L., Stebbins A., Sitwell M., 2014, ApJ, 781, 57
- Smith E. K., 1982, Radio Sci., 17, 14551465
- Staggs S. T., Jarosik N. C., Wilkinson D. T., Wollack E. J., 1996, ApJ, 458, 407
- Stompor R. et al., 2002, Phys. Rev. D, 65, 022003
- Switzer E. R. et al., 2013, MNRAS, 434, L46
- Szapudi I., Prunet S., Colombi S., 2001, ApJ, 548, L115L118
- Tatarskii V., 1961, Wave Propagation in a Turbulent Medium, Dover books on physics and mathematical physics. Dover
- Tegmark M., Eisenstein D. J., Hu W., de Oliveira-Costa A., 2000, ApJ, 530, 133
- Thompson A., Moran J., Swenson G., 2008, Interferometry and Synthesis in Radio Astronomy. Wiley
- Weinberg D. H., Mortonson M. J., Eisenstein D. J., Hirata C., Riess A. G., Rozo E., 2013, Phys. Rep., 530, 87
- White R. L., Becker R. H., Helfand D. J., Gregg M. D., 1997, ApJ, 475, 479
- Wolz L., Abdalla F. B., Blake C., Shaw J. R., Chapman E., Rawlings S., 2014, MNRAS, 441, 3271

This paper has been typeset from a \LaTeX file prepared by the author.

APPENDIX A: ATMOSPHERIC NOISE

We quantify the total contribution of the atmospheric noise in Section A1 and we discuss the contribution of the atmospheric turbulences induced by the water vapor inhomogeneities in Section A2.

A1 Total atmospheric absorption and emission

For our analysis of the effects of absorption and emission below, we consider a layer of the water vapour at a temperature T_{atm} and an optical depth τ at a given observing frequency. Around 1 GHz, the optical depth is dominated by oxygen with a small contribution from water, usually quantified with the precipitable water vapour (PWV). PWV is defined as the height of liquid water if all the water vapor would be condensed in a column of the atmosphere. Hence, it can undergo changes on a daily basis and between different sites. The total zenith optical depth can be calculated by the following relation at one frequency ν (Butler 2002)

$$\tau = 10^{-3} \times (\tau_{\text{ox}} + \tau_{\text{wv}} \text{PWV (mm)}), \quad (\text{A1})$$

where τ_{ox} is the oxygen optical depth and τ_{wv} the water vapor optical depth. These parameters are constant and depend on the frequency. We use the ATM software (Pardo, Cernicharo & Serabyn 2001) to determine their values for an altitude of the site at 200 m, a ground level pressure of ~ 1000 mbar, a water vapour scale height of 2 km and a ground level temperature $T_{\text{atm}} = 260$ K, and we find $\tau_{\text{ox}} = 7.1$, $\tau_{\text{wv}} = 0.015$. This is consistent with other predictions in the literature (Smith 1982).

The total contribution of the atmospheric emission T_{em} to the power received on one receiver is related to the optical depth by

$$T_{\text{em}} = T_{\text{atm}}(1 - e^{-\tau}). \quad (\text{A2})$$

The atmosphere leads to an attenuation of the signal from a source with a flux density S_{em} . For an average optical depth τ , the flux received by the instrument is

$$S_{\text{abs}} = S_{\text{em}}e^{-\tau}. \quad (\text{A3})$$

For $\tau \ll 1$, we obtain $S_{\text{abs}} \sim S_{\text{em}}(1 - \tau)$. Thus, the attenuation of the source by the atmosphere is at a level of one percent. For this reason, we can consider only the atmospheric emission, which is much larger than the absorption.

The atmospheric emission contributes to the system temperature of the instrument, adding to the noise from the emissions of the instrument subsystems and from the ground pick-up and sky (astronomical signal). In the case of a small optical depth $\tau \leq 0.05$, from Eq. A2, we can write $T_{\text{em}} \approx T_{\text{atm}}\tau$. The theoretical emission is given by

$$T_{\text{em}}(1 \text{ GHz}) = 1.8 + 3.9 \times 10^{-3} \text{PWV (mm)}. \quad (\text{A4})$$

In days with favourable atmospheric conditions $\text{PWV} < 2$ mm, we find $T_{\text{em}} = 1.81$ K, and in days with bad weather $\text{PWV} > 4$ mm, $T_{\text{em}} = 1.82$ K. From the models of the atmospheric emission (Danese & Partridge 1989), Staggs et al. (1996) predicts a similar contribution with $T_{\text{em}} = 1.7$ K. It varies so little because $\tau_{\text{wv}} \ll \tau_{\text{ox}}$ when the weather is stable.

A2 Atmospheric fluctuations

The fluctuating atmospheric signal in the timelines depends on the precipitable water vapour level, the turbulence height and the thickness and the wind speed of the layer. According to the Kolmogorov model of turbulence (Tatarskii 1961), we can assume that the fluctuations in water vapour occur in a turbulent layer at a height h_{av} with a thickness δh , with $h_{\text{av}} \gg \delta h$. The resulting power spectrum from the turbulence in the timelines is assumed to be a power-law with index $b = -11/3$ on small scales and $b = -8/3$ at large scales, and is given for both cases by (Lay & Halverson 2000)

$$\begin{aligned} \langle T^2(\alpha_x, \alpha_y) \rangle &= \frac{A}{\sin \epsilon} \left(\frac{h_{\text{av}}}{\sin \epsilon} \right)^{5/3} (\alpha_x^2 + \alpha_y^2)^{-11/3} \\ &\text{if } \frac{h_{\text{av}}}{2\Delta h \sin \epsilon} \ll (\alpha_x^2 + \alpha_y^2)^{1/2} \ll \alpha_{\text{inner}}, \end{aligned} \quad (\text{A5})$$

$$\begin{aligned} \langle T^2(\alpha_x, \alpha_y) \rangle &= \frac{A'}{\sin \epsilon} \left(\frac{h_{\text{av}}}{\sin \epsilon} \right)^{5/3} (\alpha_x^2 + \alpha_y^2)^{8/3} \\ &\text{if } \alpha_{\text{outer}} \ll (\alpha_x^2 + \alpha_y^2)^{1/2} \ll \frac{h_{\text{av}}}{2\Delta h \sin \epsilon}, \end{aligned} \quad (\text{A6})$$

where α_{inner} and α_{outer} are the inner and outer scales of the turbulences, Δh is the outer scale size, and ϵ is the elevation angle. The coefficients A and A' are the amplitudes of the turbulence. The parameters $\alpha_{x,y}$ are the angular wavenumbers, related to the spatial wavenumbers $k_{x,y}$ by $\alpha_{x,y} = k_{x,y}h_{\text{av}}/\sin \epsilon$.

In order to predict the residual level of the brightness temperature fluctuations for a single dish at sea level, we follow the Church model (Church 1995). We assume that the effective beam area is described by a Gaussian beam

$$A(x, y, z) = \frac{2\lambda^2 z^2}{\pi w^2(z)} \exp\left(-\frac{2(x^2 + y^2)}{w^2(z)}\right), \quad (\text{A7})$$

where $w(z) = w_0 \left(1 + \frac{\pi^2 w_0^2}{\lambda^2 z^2}\right)$.

The parameter w_0 is the beam waist radius related to the resolution θ_{FWHM} by $w_0 = \lambda \sqrt{2 \log 2} / (\pi \theta_{\text{FWHM}})$.

In the limit of a long averaging time, the Church model (Church 1995) gives the rms fluctuations in antenna temperature for a single-dish according to the outer scale L_0 by

$$\Delta T_{\text{atm}}^2 = 0.3 \sqrt{\frac{\pi}{2}} L_0^{5/3} \int_{z_1}^{z_u} C_\alpha^2(z) T_{\text{atm}}^2(z) \left(1 + \frac{w^2(z)}{2L^2}\right)^{-1} dz, \quad (\text{A8})$$

where T_{atm} is the atmosphere temperature, $L = 3L_0$, z_u is the height of the atmosphere and z_1 the breakdown of the assumption $z \gg x, y$. The parameter C_α is a measurement of the amplitude of the turbulent fluctuations and is given at 15 GHz by

$$C_\alpha^2 = 2.0 \times 10^{-14} \text{ m}^{-8/3} \exp\left(-\frac{z}{z_0}\right). \quad (\text{A9})$$

To simplify the equations, we do not take into account the effect of the wind speed as done in Lay & Halverson (2000). This adds a time dependence, which allows the measured fluctuations to decrease with larger integration times. The brightness temperature of the fluctuations induced by the water vapour molecules can be scaled to other frequencies, based on the emissivity spectrum of water vapour. The water vapour spectrum is composed of spectral emission lines overlaid on a background emission, which increases as the square of the frequency (Smith 1982), so we scale Eq. A8 as our frequency of observation to the fourth power. We assume a model of the telescope with $\theta_{\text{FWHM}} = 40$ arcmin at 1 GHz, a temperature of the atmosphere of $T_{\text{atm}} = 270$ K and a maximum height of 2 km. We use the value suggested in Church (1995) for $L_0 = 10$ m. With these assumptions, we find $\Delta T_{\text{atm}} \sim 0.01$ mK.